



Highly accessible and stable Co-based active sites enabled by 2D/3D dual-confined strategy for Zn-air batteries

Jinping Zhang^{a,b,*}, Zhiyuan Mei^c, Lilan Yi^a, Jinshu Tian^d, Kejian Li^e, Xincheng Hu^a, Yong-Ya Zhang^{a,b,*}, Rui Wang^b, Hong Guo^c, Shuang-Quan Zang^{b,**}

^a Henan Engineering Center of New Energy Battery Materials, College of Chemistry and Chemical Engineering, Shangqiu Normal University, Shangqiu 476000, China

^b Henan Key Laboratory of Crystalline Molecular Functional Materials, Green Catalysis Center, and College of Chemistry, Zhengzhou University, Zhengzhou 450001, China

^c School of Materials and Energy, Yunnan University, Kunming 650091, China

^d College of Chemical Engineering, Zhejiang University of Technology, Hangzhou 310014, China

^e School of Metallurgy and Materials Engineering, Chongqing University of Science and Technology, Chongqing 401331, China

ARTICLE INFO

Keywords:

2D/3D dual-confined strategy
Poly(ionic liquid)
Oxygen reduction reaction
Zn-air batteries

ABSTRACT

The rational design and facial preparation of highly accessible nanocatalysts that are stable against sintering is a crucial concern in heterogeneous electrocatalysis. Here, an effective and high-stable Co-based heterogeneous electrocatalyst with sufficient exposure of active species was prepared by dual-confined strategy with 3D ZIF-8 frameworks and 2D lamellar poly(ionic liquid) (PIL) networks. As cathode catalyst for Zn-air battery, the as-obtained Co-ZIF8-PIL-800 catalyst displayed excellent oxygen reduction reaction (ORR) performance ($E_{1/2} = 0.87$ V), high specific capacity ($810.9 \text{ mA h g}_{\text{Zn}}^{-1}$) and superior stability than that of Pt/C and RuO_2 benchmark. Structure-activity relationship proved that the dispersion of 3D ZIF frameworks in 2D PIL networks ensured the durability of Co-ZIF8-PIL-800, and the confinement of Co species in 2D/3D composite hierarchical frameworks increased the exposure of active sites. The excellent electrocatalytic efficiency of Co-ZIF8-PIL-800 implied the great potential of this 2D/3D dual-confined strategy in constructing highly efficient electrocatalysts.

1. Introduction

The design and fabrication of efficient and stable electrocatalysts have been a critical topic for heterogeneous electrocatalysis which plays an important role in the energy conversion and utilization [1–6]. Much exciting process has been made in the improvement of the catalytic performance by accurately regulating and optimizing the active centers in catalysts such as increasing the exposure and enhancing the intrinsic activity of active sites [7–10]. However, the increase of activity for electrocatalysts normally results in the decrease of stability, which is an important contradiction in catalytic science and industrial applications [6,11,12]. The loss of activity during reaction could essentially attributed to (1) the deactivation of active sites [13–15], including decomposition, poisoning, migration, aggregation, etc., and/or (2) the collapse/sintering of the supports so that to decrease the exposure degree of active sites [16,17]. Due to the vital role of the active sites played

in determining the catalytic efficiency, too much attention was paid to the development of active centers themselves, often ignoring the important role of the structural stability of the supports.

The catalyst supports, especially carbon-based supports, played an important role in heterogeneous electrocatalysis due to the advantages of light-weight, conductivity, abundance, high porosity, and high stability [18]. As one of the most important carbon-based supports, porous carbon supports can fully expose the active sites of the catalyst, improve catalyst utilization and mass transfer [19,20]. The advantages of porous carbon-based materials are determined by carbon precursors and preparation methods [21]. For example, 3D ZIF materials, a kind of ideal carbon precursors attributed to the unique highly porous structure and easily functionalization, have been widely applied in fabricating the N doped carbon supported metal-based catalysts with high exposure degree [22–24]. Although remarkable results have been achieved by using high porous ZIFs as the precursors to disperse the active species, the

* Corresponding author at: Henan Engineering Center of New Energy Battery Materials, College of Chemistry and Chemical Engineering, Shangqiu Normal University, Shangqiu 476000, China.

** Corresponding author.

E-mail addresses: zhangyongya_1990@126.com (Y.-Y. Zhang), zangsqzg@zzu.edu.cn (S.-Q. Zang).

<https://doi.org/10.1016/j.apcatb.2023.123044>

Received 5 April 2023; Received in revised form 5 June 2023; Accepted 23 June 2023

Available online 25 June 2023

0926-3373/© 2023 Elsevier B.V. All rights reserved.

unavoidable particle fusing and support collapse during contact make it difficult to maintain the activity of these catalysts when they are used repeatedly [13,25,26]. Highly ordered graphitized carbon materials, as another important kind of carbon-based supports, are more stable, but they usually result in low surface area and insufficient porosity, which is detrimental to mass transfer [25,27]. Therefore, how to balance the relationship between stability and porosity of the carbon support and greatly enhance the catalytic efficiency of the catalyst is a key concern in the catalytic field.

Recently, 2D lamellar poly(ionic liquid) (PIL), prepared by cross-linking reaction of ionic liquid (IL), as the precursor to disperse and stabilize metal particle via one-step pyrolysis has been positively attempted in our previous work [28,29]. IL monomers composed entirely of cations and anions showed unique compatibility with ionic type metal precursors than traditional neutral monomers (such as N, N'-methylene bisacrylamide and divinylbenzene), and the PIL-to-carbon conversion can in-situ generate 2D graphitized carbon networks to prevent or delay the grow rate of metal particles. To construct an ideal electrocatalyst considering the stability of carbon supports and full exposure of active sites together, an efficient strategy is to in-situ embed the granular 3D porous frameworks into the 2D lamellar networks, rather than the traditional carbon coating or loading, to isolate each of the porous frameworks so as to limit the migration of active species and agglomeration of porous frameworks. This dual confined structure of active sites @ 3D porous frameworks @ in-situ 2D lamellar networks will be beneficial to the exposure of active sites and the enhancement of catalyst durability.

Herein, as a proof-of-concept experiment, we propose and demonstrate the dual-confined strategy to confine Co species into 3D ZIF-8 frameworks and jointly be embedded into 2D lamellar poly(ionic liquid) (PIL) networks to prepare Co @ ZIF-8 @ in-situ PIL-type catalysts named as Co-ZIF8-PIL-T (T represents the annealing temperature) for the rechargeable metal-air batteries which are receiving widespread attentions to alleviate the energy crisis and environmental pollution. ZIF-8 composed of Zn ion and 2-methylimidazole linker has high specific surface area ($\sim 1400 \text{ m}^2 \cdot \text{g}^{-1}$) and abundant pore structure. Co doped ZIF-8 was homogeneously introduced into the IL monomer solution, following by in-situ crosslinked polymerization reaction to confine ZIF-8 particles into lamellar PIL networks. During the calcination process, the 3D ZIF-8 framework could be maintained and isolated by each other due to the confinement effect of the in-situ derived PIL-carbon networks. Meanwhile, the evaporation of Zn could generate abundant mesopore structure in the carbon support to facilitate the mass transfer. When applied in oxygen electrocatalysis, the as-obtained Co-ZIF8-PIL-800 catalyst exhibits comparable oxygen reduction reaction (ORR) activity ($E_{1/2} = 0.87 \text{ V}$) and superior stability to that of commercial Pt/C (20 wt %) under alkaline conditions. As an oxygen cathode catalyst of Zn-air batteries (ZABs), Co-ZIF8-PIL-800 displays excellent ORR/oxygen evolution reaction (OER) activity with potential difference of 0.82 V between the OER ($E_{j=10}$) and ORR ($E_{1/2}$), higher special capability ($810.9 \text{ mA h} \cdot \text{g}_{\text{Zn}}^{-1}$), and superior stability than that of commercial Pt/C and RuO_2 catalysts.

2. Experimental

2.1. Chemicals and reagents

5% H_2/Ar gas mixture as purchased from Longhai Factory. Vinyl imidazole, 2-methylimidazole (MeIM), dibromoethane, 2, 2'-azobis (2-methylpropionamide) dihydrochloride (AIBA) initiator were supplied by J&K. The commercial Pt/C catalyst (20 wt% Pt) was sourced from Macklin. All other chemicals and solvents were provided by the local suppliers. All experimental water was obtained by an ultrapure water purification system.

2.2. Catalysts preparation

2.2.1. Synthesis of ionic liquid monomer N, N-ethylene bisvinylimidazole bromide (EBVImBr)

Vinyl imidazole (5.64 g, 60 mmol) and dibromoethane (5.63 g, 30 mmol) were dissolved in ethyl acetate (50 mL), respectively. The reaction was refluxed under magnetic stirring for 12 h, and a large amount of white solid was precipitated. After reaction, it was naturally cooled to room temperature, washed with ethyl acetate for 2–3 times and dried by rotary evaporation. The white powder solid was obtained in a 98% yield.

^1H NMR (400 MHz, D_2O , TMS) δ (ppm): 9.11 (s, 2 H), 7.82 (s, 2 H), 7.54 (s, 2 H), 7.10 (dd, $J = 16.0, 8.0 \text{ Hz}$, 2 H), 6.10 (dd, $J = 8.0, 4.0 \text{ Hz}$, 2 H), 5.51 (dd, $J = 8.0, 4.0 \text{ Hz}$, 2 H), 4.81 (s, 4 H); ^{13}C NMR (100 MHz, D_2O , TMS) δ (ppm): 135.85, 127.94, 122.53, 120.95, 111.56, 59.26.

2.2.2. Synthesis of N doped graphene oxide (NGO)

2 mL of 25% ammonia water was dropped into the 50 mL of $4.0 \text{ mg} \cdot \text{mL}^{-1}$ GO dispersion. Then, the above solution was poured into a Teflon-lined autoclave and heat-treated at 175°C for 24 h. Finally, the sediment was centrifuged by using distilled water until pH = 7 and dried at 100°C over night to obtain black powder NGO.

2.2.3. Synthesis of Co-PIL-T and PIL-800

EBVImBr (1.504 g) was dissolved in 3 mL H_2O in a 50 mL round-bottom flask. Then $\text{CoCl}_2 \cdot 6 \text{ H}_2\text{O}$ (0.104 g) was added into the ionic liquid and stirred at 60°C for 2 h to form a homogeneous solution. Subsequently, the AIBA initiator (75 mg) was poured to promote the polymerization of ionic liquid at 60°C overnight. The obtained polymer was pyrolyzed at different temperature ranging from 600°C , 700°C , 800°C and 900°C under 5% H_2/Ar atmosphere, respectively. The carbonized materials were marked as Co-PIL-T, where T meant the annealing temperature. As the control sample, PIL-800, without the addition of Co salt, was obtained by pyrolyzing PIL at 800°C under 5% H_2/Ar atmosphere.

2.2.4. Synthesis of ZIF-8, Co doped ZIF-8 (Co-ZIF-8) and ZIF-67 particles

ZIF-8 crystal was prepared as follows: $\text{Zn}(\text{NO}_3)_2 \cdot 6 \text{ H}_2\text{O}$ (0.558 g) and MeIM (0.616 g) were dissolved in 15 mL methanol, respectively. The $\text{Zn}(\text{NO}_3)_2 \cdot 6 \text{ H}_2\text{O}$ solution was added dropwise into the MeIM solution under vigorous stirring to generate the white precipitate. After 24 h reaction at room temperature, the white ZIF-8 crystal was obtained by the centrifugation using methanol and dried for 8 h at 80°C .

Co-ZIF-8 was prepared by the solvothermal method. Typically, the $\text{CoCl}_2 \cdot 6 \text{ H}_2\text{O}$ (0.010 g) and ZIF-8 (0.100 g) were mixed in ethanol solution overnight at 80°C and then the obtained bluish violet powder was collected by centrifugation, washed using methanol and dried for 8 h at 80°C .

ZIF-67 was synthesized by the following method: $\text{Co}(\text{NO}_3)_2 \cdot 6 \text{ H}_2\text{O}$ (0.291 g) and MeIM (0.328 g) were dissolved in 25 mL methanol, respectively. Both the solutions were mixed to generate the purple precipitate. The purple product was centrifuged, washed and dried to obtain the ZIF-67 crystal.

2.2.5. Synthesis of Co-ZIF8-PIL-T

ZIF-8 crystal, $\text{CoCl}_2 \cdot 6 \text{ H}_2\text{O}$ and ionic liquid were dispersed into the 3 mL water and ethanol (water/ethanol = 1/2, v/v) mixed solvents and stirred at 60°C for 2 h. Then the initiator AIBA was added into the mixture and the polymerization was executed at 80°C for 12 h to form the bulk polymer composite. The polymer was pyrolyzed at 700°C , 800°C and 900°C for 6 h under 5% H_2/Ar atmosphere to prepare the catalyst, which marked as Co-ZIF8-PIL-T. Similarly, the ZIF8-PIL polymer precursor was prepared without the Co salt. After calcination at 800°C under 5% H_2/Ar atmosphere, the ZIF8-PIL-800 was obtained.

2.2.6. Synthesis of ZIF8-800, Co-ZIF8-800 and ZIF67-800

Similar, the ZIF8-800, Co-ZIF8-800 and ZIF67-800 catalysts were

synthesized by pyrolyzing the ZIF-8, Co-ZIF-8 and ZIF-67 crystals at 800 °C for 6 h under 5% H₂/Ar atmosphere.

2.2.7. Synthesis of Co-ZIF8-NGO-800

ZIF-8 crystal, CoCl₂·6 H₂O and NGO were dispersed into the 10 mL water and ethanol (water/ethanol = 1/2, v/v) mixed solvents and stirred at the room temperature for 48 h. Then the mixture was cooled by using liquid nitrogen and dried for 72 h under vacuum to acquire the black fluffy powder. The as-obtained powder precursor was pyrolyzed at 800 °C for 6 h under 5% H₂/Ar atmosphere to produce Co-ZIF8-NGO-800 catalyst. The Co loading in Co-PIL-800, Co-ZIF8-PIL-800 and Co-ZIF8-NGO-800 was measured by ICP-OES.

3. Results and discussion

3.1. Crafting of dual confined Co-based catalysts

The divinyl functionalized IL monomer was facilely prepared by the one-step ionization of vinyl imidazole with dibromoethane and characterized by ¹H NMR and ¹³C NMR (Scheme S1, Figs. S1 and S2). Co-based catalysts with dual-confined structure were constructed via in-situ polymerization and carbonation strategy. As illustrated in Fig. 1a, Co salts was firstly reacted with ZIF-8 efficiently to ensure Co²⁺ to be homogeneously adsorbed/doped into the 3D ZIF-8 frameworks, and then dispersed into the solution of IL monomer. The in-situ polymerization was triggered subsequently by the free radical initiator 2,2'-azobis [2-methylpropionamide] dihydrochloride (AIBA) to generate 2D

lamellar poly(ionic liquid) (PIL) networks. The 2D/3D structured Co@ZIF-8 @in-situ PIL composite, in which Co²⁺ and ZIF-8 particles were both confined into PIL networks, was finally pyrolyzed at the set temperature under the H₂/Ar atmosphere to obtain the Co-ZIF8-PIL-800 catalyst. Attributed to the synergistic effect of 2D/3D composite structure during the calcination, the in-situ generated Co species should be confined in ZIF-8/PIL derived hierarchical frameworks and the PIL derived 2D carbon networks are expecting to prevent the fusing of ZIF derived particles and reinforce the robustness of the catalyst.

3.2. Morphology and microstructures

Scanning electron microscope (SEM) combined with energy-dispersive X-ray spectrometry (EDS) mapping analysis were firstly adopted to investigate the morphology and element distribution of Co-ZIF8-PIL-800 catalyst. As shown in Fig. 1b and Fig. S3, the polyhedral particles were uniformly dispersed in the 2D lamellar carbon networks without particle fusing and Co element was mainly distributed in polyhedral particles. The size of polyhedral particles ranged from 50 to 210 nm with the average of ~115 nm, which was consistent with the average size of ZIF-8 and ZIF8-800 (~130 nm) (Fig. S4). This implied that the polyhedral particles were most probably derived from the pyrolysis of ZIF frameworks in the catalyst precursor Co@ZIF-8 @in-situ PIL. Further evidence was obtained by designing the control samples Co-ZIF8-800, PIL-800 and ZIF8-PIL-800, and comparing the morphology with Co-ZIF8-PIL-800. As can be seen from Fig. S5, without the addition of IL, Co-ZIF8-800 showed the similar morphology as the ZIF8-800 with

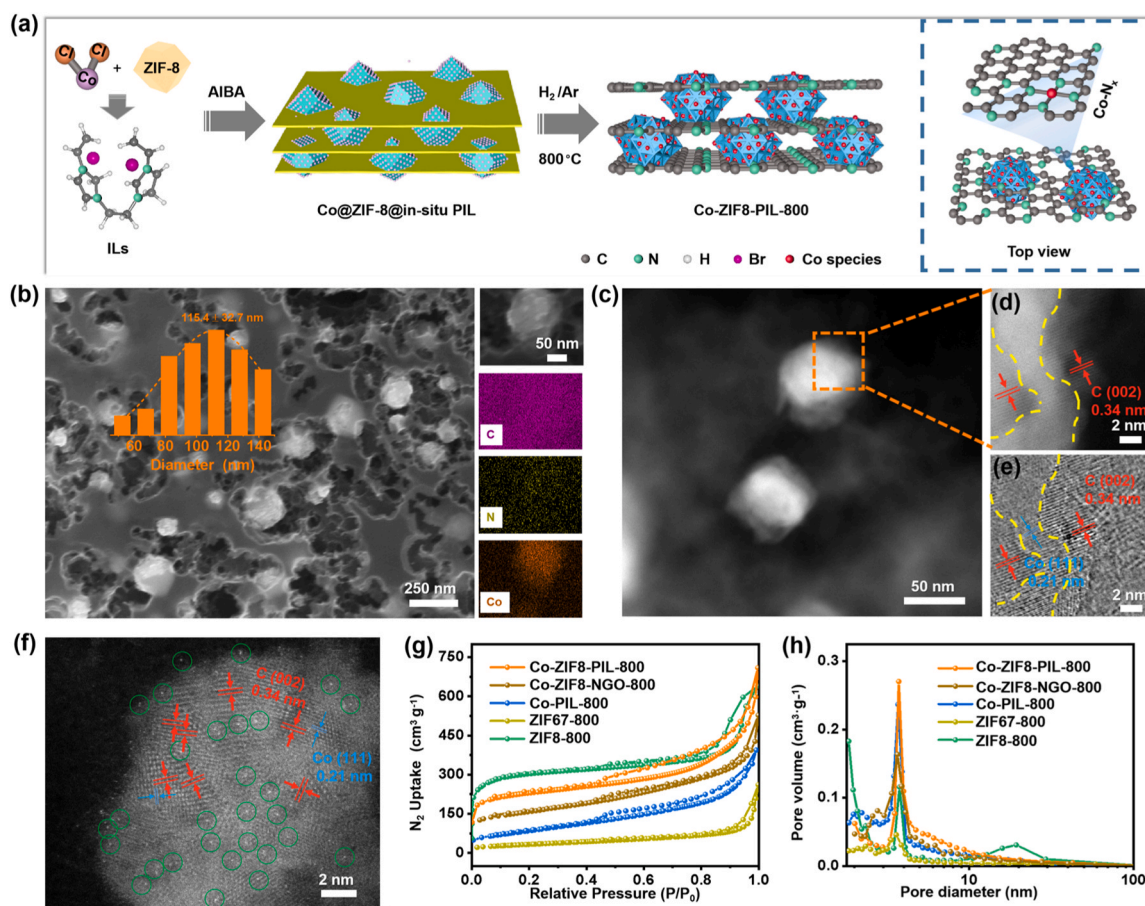


Fig. 1. Schematic synthesis and structure characterization of the dual-confined Co-ZIF8-PIL-800 and the comparative catalysts. (a) Graphical description of the synthetic methodology of Co-ZIF8-PIL-800 catalyst. (b) SEM image and EDS mapping, (c, d) HAADF-STEM, (e) IDPC-STEM image of Co-ZIF8-PIL-800 catalyst, (f) HAADF-STEM image of Co-ZIF8-PIL-800 catalyst after acid washing. (g) N₂ adsorption and desorption isotherms and (h) pore distribution of Co-ZIF8-PIL-800, Co-ZIF8-NGO-800, Co-PIL-800, ZIF67-800 and ZIF8-800 catalysts.

partial structural shrinkage during the calcination process. When PIL was introduced without the addition of Co^{2+} , polyhedral particles could be observed in ZIF8-PIL-800 compared to PIL-800 with only 2D carbon sheets (Figs. S6 and S7). These results proved the stability of ZIF-derived porous frameworks in the presence of Co^{2+} and IL during calcination, and further implied the efficiency of 2D/3D dual-confined strategy that isolated each of the ZIF particle to prevent sintering. It is worth noting that pure PIL derived carbon materials show relatively thick layer structure without exfoliation (the thickness of PIL-800 sheets is $\sim 1 \mu\text{m}$ as shown in Fig. S6c). When Co doped ZIF-8 frameworks are in situ confined inside the PIL networks, the evaporation of Zn during the pyrolysis process foam the composite and exfoliate the 2D PIL in some extent, resulting in relatively thinner 2D PIL layers in Co-ZIF8-PIL-800 than PIL-800 sheets.

High-angle annular dark-field scanning transmission electron microscopy (HAADF-STEM) images (Fig. 1c and d) combined with integrated differential phase-contrast scanning transmission electron microscopy (iDPC-STEM) image (Fig. 1e) further confirmed the dispersion of Co species on the surface of polyhedral ZIF frameworks. The lattice distance of 0.34 nm and 0.21 nm should be assigned to the (002) plane of carbon supports and the (111) plane of Co particles, respectively, coincident with the results of powder X-ray diffraction (XRD) analysis (Fig. S8). For Co-ZIF8-PIL-800 catalyst after acid washing, atomically dispersed Co sites were observed by HAADF-STEM, and distinct lattice fringes with the lattice spacing of 0.34 nm belonging to the lattice fringes of carbon support were seen (Fig. 1f) [30]. Besides, faint lattice fringes with the lattice spacing of 0.21 nm were observed, which may be attributed to the trace amount of unexposed Co nanoparticles deeply buried in the carbon layer that have not been washed away [31]. Based on the HAADF-STEM analysis results of the catalyst before and after acid washing, it could be concluded that Co particles and atomic Co are coexisted in Co-ZIF8-PIL-800 catalyst.

Besides, other Co-based catalysts with mono-confined and non-confined structures were prepared to demonstrate the advantage of dual-confined strategy. The traditional carbon loading catalyst (Co-ZIF8-NGO-800) was prepared by impregnation of Co doped ZIF-8 on NGO and pyrolysis at the same condition as Co-ZIF8-PIL-800. Meanwhile, the mono-confined catalysts (Co-PIL-800 and ZIF67-800) were prepared by carbonization of Co-based PIL gel and ZIF-67, respectively. ZIF8-800 was also achieved by direct pyrolysis of ZIF-8 as a blank control experiment. As observed by STEM and TEM images, the sintering of polyhedral particles was serious in ZIF8-800 sample (Fig. S4). After coated by layered NGO, particle fusing still partially existed due to the weak confinement effect of traditional carbon loading method (Fig. S9). The aggregation of Co particles was observed for the Co-PIL-800 and ZIF67-800 catalysts prepared through mono-confined strategy (Figs. S10 and S11). It proved that the dual-confined strategy of 2D lamellar PIL and 3D ZIF-8 frameworks was beneficial to the structural stability, the homogeneous dispersion and exposure of Co-based active species. In addition, N_2 adsorption and desorption measurements were performed to disclose the porosity and specific surface area of the catalysts, which are crucial for the accessibility of active species. As showed in Fig. 1g and h, the BET surface areas of Co-ZIF8-PIL-800 was $719 \text{ m}^2 \cdot \text{g}^{-1}$, slightly lower than that of 3D ZIF8-800 framework ($928 \text{ m}^2 \cdot \text{g}^{-1}$) but obviously higher than that of the carbon loading catalyst Co-ZIF8-NGO-800 ($479 \text{ m}^2 \cdot \text{g}^{-1}$), and the mono-confined catalysts ZIF67-800 ($119 \text{ m}^2 \cdot \text{g}^{-1}$) and Co-PIL-800 ($315 \text{ m}^2 \cdot \text{g}^{-1}$). The pore size of different catalysts was all distributed in mesoporous range (about 3–4 nm) and Co-ZIF8-PIL-800 showed the largest mesoporous volume (Table S1). This might be attributed to that when ZIF-8 frameworks were confined in PIL networks, the evaporation of Zn during pyrolysis partially penetrated through the PIL layer and generated the abundant mesopore, which could increase the exposure of active sites and promote the mass transfer during the catalytic reaction.

3.3. Chemical composition and electronic structure characterization

The surface composition and chemical state of the catalysts prepared by mono- and dual-confined strategy were detected by XPS characterizations. The typical XPS survey spectra showed the coexistence of C, N, O and Co elements on the surface of Co-PIL-800, ZIF67-800 and Co-ZIF8-PIL-800 (Fig. 2a, Tables S2 and S3) [32]. As shown in Fig. 2b and c, the C1s spectra were divided into $\text{C}=\text{C}$ (284.6 eV), $\text{C}=\text{N}$ (285.4 eV) and $\text{C}=\text{N}$ (289.1 eV) species [33,34]. The N 1s spectra were fitted into four peaks located at ~ 398.6 , ~ 399.8 , ~ 401.2 , ~ 405.2 eV, which corresponded to the pyridinic-N, pyrrolic-N, graphitic-N, and N-oxide, respectively [33,35]. The high resolution profile of Co 2p in Co-ZIF8-PIL-800 catalyst at 780.5 and 796.0 eV with a separation of 15.5 eV was categorized as Co $2\text{p}_{3/2}$ and Co $2\text{p}_{1/2}$ peak, respectively (Fig. 2d) [36,37]. The negative shift of energy binding had been observed compared with Co-PIL-800 (781.0 and 796.8 eV) and ZIF67-800 (781.8 and 797.2 eV) catalysts. It signified that the composite structure of 3D ZIF-8 frameworks and 2D carbon layer could alter the interaction between the Co species and carbon structure. The deconvoluted Co $2\text{p}_{3/2}$ spectra of all the catalysts were fitted into three different kinds of Co sites at ~ 778.8 , ~ 780.8 and ~ 782.3 eV. The characteristic peak at ~ 778.8 eV indicated the existence of metallic state Co^0 . The Co $2\text{p}_{3/2}$ signals at ~ 780.8 and ~ 782.3 eV, together with the satellite peaks located at ~ 787.1 eV, were assigned to the Co^{II} species which might exist in the catalysts in the form of Co-O_x and Co-N_x species [38]. It was believed that Co particles and Co-O_x showed outstanding OER performance with the excellent electrical conductivity [39] and the Co-N_x moiety have emerged as main ORR active sites comparable to that of commercial Pt/C catalyst [13], Co-ZIF8-PIL-800 should have great potential in enhancing the ORR/OER activity when assembled as Zn-air batteries.

The surface defect of carbon matrix and 3d orbital electron configuration of Co species were investigated by Raman spectra, electron paramagnetic resonance (EPR) and zero-field cooling temperature-dependent magnetic susceptibility (M-T) measurements. Raman spectra were displayed in Fig. S12 to probe into the defect degree of carbon structure. The peak intensity ratio of the D (defective carbon) band at 1345 cm^{-1} and G (graphitic carbon) band at 1585 cm^{-1} (I_D/I_G) for Co-ZIF8-PIL-800 was higher than that of Co-PIL-800, illustrating that the dual-confined strategy of 3D ZIF-8 framework and 2D lamellar PIL networks generated more defective sites compared with mono-confined catalyst Co-PIL-800 [26,28]. EPR spectra were employed to reflect the coordination environment of Co species in the catalysts (Fig. S13). The broad resonance signals at $g \approx 5$ could be assigned to Co^{II} species ($3d^7$) in Co-N_4 species and the major peak at $g \approx 2$ validated the presence of defects commonly associated with unpaired electrons [40–42]. M-T measurement was carried out to investigate the molar magnetic susceptibility (χ_m) patterns and the average number of unpaired Co 3d orbital electrons (n) in Co-N_4 species [9,43]. As shown in Fig. 2e, the unpaired electron number of Co 3d orbit in Co-ZIF8-PIL-800 ($n \approx 2.63$) and Co-PIL-800 ($n \approx 2.92$) were both less than high spin state of Co 3d orbit ($n = 3$). According to the crystal field theory of coordination compounds and Jahn-Teller effect, the state of Co^{II} species in Co-ZIF8-PIL-800 should be a combined state where high spin state and low spin state coexist as illustrated in the Fig. 2f, implying that the Co-N_4 species in Co-ZIF8-PIL-800 was more stable with lower energy [9]. This coexisted electron spin configuration of Co^{II} species could enhance the interaction of Co-N and O_2 molecular [10]. These results indicated that the dual-confined strategy not only facilitates the dispersion and exposure of Co species, but also modulates the surface defect of catalyst and the electronic configuration of active Co species, which implied the potential of Co-ZIF8-PIL-800 in electrocatalytic activation and reduction of oxygen.

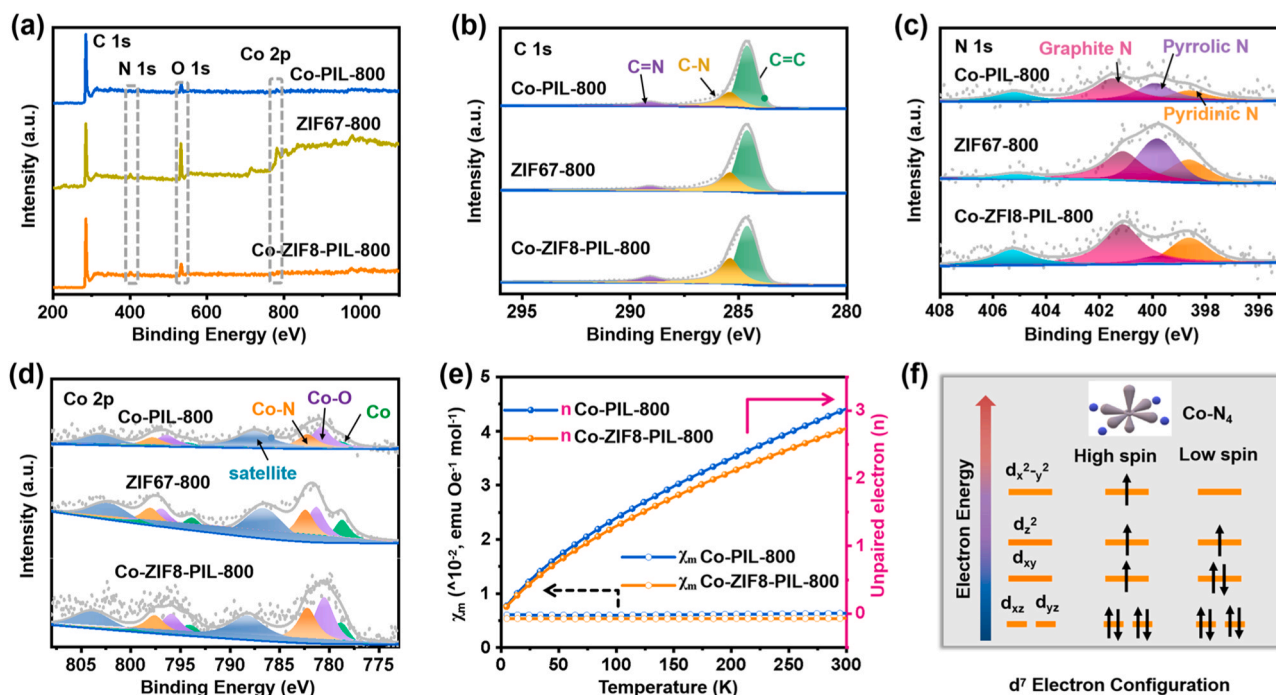


Fig. 2. Analysis of the chemical composition and electronic structure of the catalysts. (a) XPS survey spectra of Co-ZIF8-PIL-800, ZIF67-800 and Co-PIL-800 catalysts. High-resolution XPS spectra of (b) C 1s, (c) N 1s and (d) Co 2p XPS spectra of Co-ZIF8-PIL-800, ZIF67-800 and Co-PIL-800, respectively. (e) M-T curves and the calculated number of the unpaired electrons in the Co 3d orbitals of Co-ZIF8-PIL-800 and Co-PIL-800 catalysts. (f) Schematic illustration of energy level splitting of 3d Co orbit in Co-N₄ species.

3.4. Electrocatalytic performance of Co-ZIF8-PIL-800

3.4.1. ORR activity

The ORR performance of the as-prepared catalysts and commercial Pt/C with 20 wt% Pt were evaluated by using a rotating disk electrode

(RDE) configuration performed under 0.1 M KOH electrolyte. The influence of annealing temperature on the catalytic activity was investigated firstly. For Co-PIL-T where T ranging from 700 °C to 900 °C, the linear sweep voltammetry (LSV) curve of Co-PIL-800 at 1600 rpm showed the biggest half-wave potential ($E_{1/2}$) (0.76 V) compared to Co-

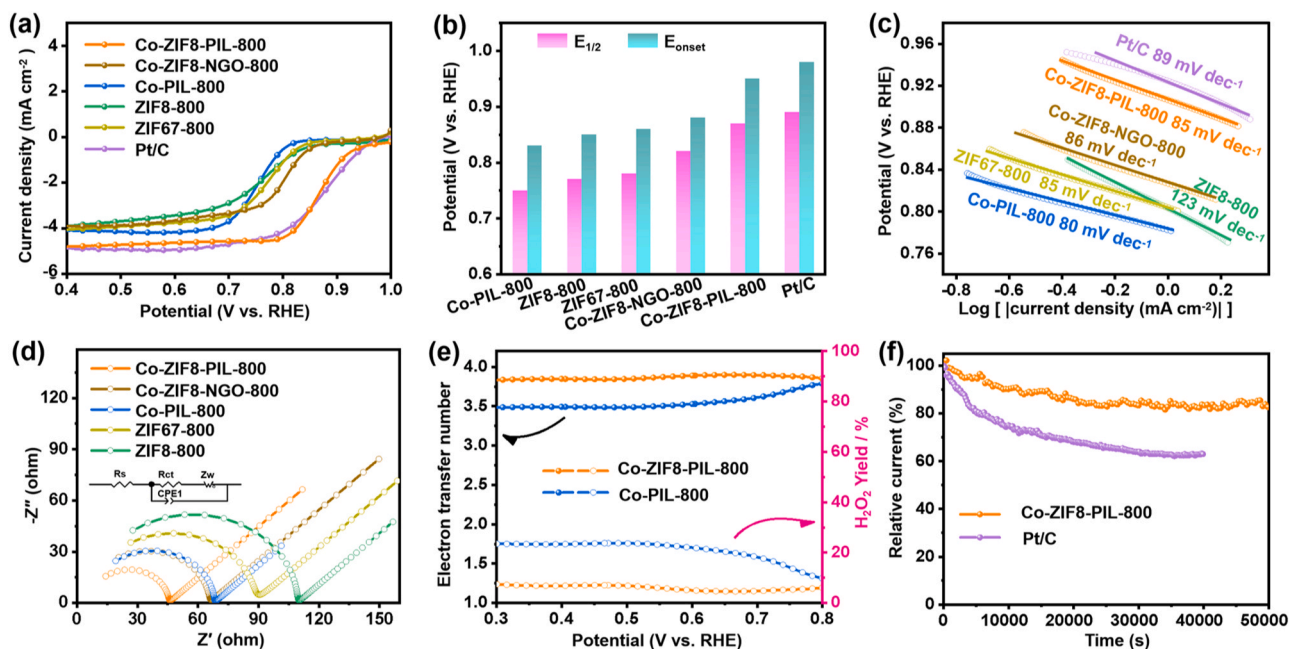


Fig. 3. Evaluation of ORR performance in O₂-saturated 0.1 M KOH solution. (a) ORR LSV curves at a scan rate of 5 mV s⁻¹ of Co-ZIF8-PIL-800, Co-ZIF8-NGO-800, ZIF67-800, Co-PIL-800, ZIF8-800 and Pt/C at the rotation speed of 1600 rpm, and (b) the corresponding onset potential (E_{onset}) and half-wave potential ($E_{1/2}$), and (c) Tafel slope. (d) Nyquist plots of Co-ZIF8-PIL-800, Co-ZIF8-NGO-800, ZIF67-800, Co-PIL-800 and ZIF8-800 with the corresponding equivalent circuit (inset). (e) Electron transfer number and H₂O₂ yield of Co-PIL-800 and Co-ZIF8-PIL-800 measured at a scan rate of 5 mV s⁻¹ at the rotation speed of 1600 rpm. (f) Chronoamperometric test curves of Co-ZIF8-PIL-800 and Pt/C at 0.65 V vs. RHE under stirring for 50000 s.

PIL-700 (0.73 V) and Co-PIL-900 (0.61 V) (Fig. S14a and S14b). It can be deduced that 800 °C was the optimal temperature for the pyrolysis of catalyst precursors. When ZIF-8 were introduced, the ORR performance of Co-ZIF8-PIL-800 was still the optimal (Fig. S15), which indicated that the ideal annealing temperature for this kind of Co-based catalysts prepared by 2D/3D dual-confined strategy was 800 °C. At the optimized annealing temperature, the ORR performance of different catalysts and commercial Pt/C was compared in detail by the LSV measurement under the same testing condition. As shown in Fig. 3a and b, the onset potential (E_{onset}), half-wave potential, and limiting diffusion current density (J_d) of Co-ZIF8-PIL-800 were 0.95 V, 0.87 V, and 4.8 mA·cm⁻², respectively, which were comparable to that of the commercial Pt/C (0.98 V, 0.89 V, 4.9 mA·cm⁻²), superior to that of blank catalyst ZIF8-800 (0.85 V, 0.77 V, 3.9 mA·cm⁻²), mono-confined catalysts Co-PIL-800 (0.83 V, 0.76 V, 4.2 mA·cm⁻²) and ZIF67-800 (0.86 V, 0.78 V, 4.1 mA·cm⁻²). Noteworthy, the ORR performance of Co-ZIF8-PIL-800 were also obviously higher than that of carbon loading catalyst Co-ZIF8-NGO-800 (E_{onset} = 0.88 V, $E_{1/2}$ = 0.82 V, J_d = 4.1 mA·cm⁻²) with ZIF-8 framework loaded on similar layered nitrogen-doped graphene and similar Co loading (Table S4). It proved that the in-situ confined polymerization technique showed significant advantages on the stabilization and dispersion of ZIF-8 framework than traditional carbon loading strategy. The Tafel slopes based on the corresponding LSV curves were plotted to evaluate the ORR kinetics of the catalysts (Fig. 3c). Co-ZIF8-PIL-800 showed the Tafel slope of 85 mV dec⁻¹, which was approximate with that of Co-PIL-800 (80 mV dec⁻¹), ZIF67-800 (85 mV dec⁻¹), Co-ZIF8-NGO-800 (86 mV dec⁻¹) and commercial Pt/C (89 mV dec⁻¹), much lower than that of ZIF8-800 (123 mV dec⁻¹). In addition, Co-ZIF8-PIL-800 delivered smaller charge transfer resistance (R_{ct}) value (38.9 Ω) than the other catalysts (Fig. 3d), implying that the dual-confined strategy of 2D PIL and 3D ZIF-8 frameworks could display the faster electron transfer kinetics than mono-confined catalysts and traditional loading catalyst. The electrochemical double-layer capacitance (C_{dl}) based on cyclic voltammetry (CV) measurements at different scan rates was obtained to estimate the electrochemical surface area (ECSA) (Fig. S16). The calculated C_{dl} value of Co-ZIF8-PIL-800 was 16.0 mF cm⁻², which was higher than that of commercial Pt/C (14.3 mF cm⁻²), Co-ZIF8-NGO-800 (13.1 mF cm⁻²), Co-PIL-800 (13.2 mF cm⁻²), and ZIF67-800 (5.3 mF cm⁻²), implying that the dual-confined strategy of 2D PIL and 3D ZIF-8 frameworks could provide more abundant accessible active sites in Co-ZIF8-PIL-800. Based on the analysis of ORR performances, BET surface area and TEM images, it could be inferred that the enhancement of catalytic efficiency after dual-confinement was ascribed to the generation of hierarchical pore structure and the increased exposure of active sites. The number of electron transfer and H₂O₂ yield in ORR process was also determined by the Koutecky-Levich (K-L) equation and rotating ring disk electrode (RRDE) measurements to judge the reaction route. As depicted in Fig. 3e and Fig. S17, the calculated electron transfer number of Co-ZIF8-PIL-800 was closest to 4 and the H₂O₂ yield was the lowest (< 10%) among the as-compared catalysts, indicating a perfect four electron transfer process on the surface of Co-ZIF8-PIL-800 catalyst. Besides, the durability of the catalysts was assessed by amperometric i-t curve measurement, XPS and STEM analysis before and after the recycling (Fig. 3 f and Fig. S18). Co-ZIF8-PIL-800 displayed excellent stability with the relative current retention of ~83% after 50000 s. In contrast, the retention of relative current on commercial Pt/C catalyst dropped to ~60% after 40000 s, indicating the great potential of Co-ZIF8-PIL-800 as cathode catalyst in practical applications of metal-air batteries and fuel cells.

3.4.2. The intrinsic activity of active species

The geometric activity related to $E_{1/2}$ and J_d is a convenient metric for comparing the ORR activity of the as-prepared catalysts, but ignores the fact that the catalytic reaction is a surface process, in which only surface active sites are involved. In order to understand the intrinsic ORR electrocatalytic activity of active species, it is necessary to estimate

the accessible gravimetric active site density (MSD) and the site activity of Co-N_x at a certain voltage [44]. Because SCN⁻ anion could poison Co center in Co-N_x active species through the formation of stable chelate complex between them, KSCN tolerance test was carried out to identify the role of Co-N_x active species in electrocatalytic oxygen reduction [45, 46]. As shown in Fig. S19, when a small amount of KSCN was added to the electrolytes, the geometric current density of the catalysts reduced significantly, indicating that the high ORR activity was derived from the atomic Co-N_x sites. The $E_{1/2}$ values of Co-ZIF8-PIL-800 catalyst was negatively shifted by ~53 mV after poisoning, higher than the shift amplitude of other Co-based catalysts, implying more accessible Co-N_x sites in Co-ZIF8-PIL-800. The gravimetric active site density (MSD) of Co-N_x species, values based on the number of accessible Co-N_x sites normalized to the mass of the catalysts, was further calculated by nitrite reductive stripping method [47,48]. Co-ZIF8-PIL-800 possessed the highest MSD of ~2 μmol·g⁻¹, which was much higher than that of Co-ZIF8-NGO-800 (0.63 μmol·g⁻¹), ZIF67-800 (0.35 μmol·g⁻¹) and Co-PIL-800 (0.27 μmol·g⁻¹), respectively (Fig. S20). These results indicated that the 2D/3D dual-confined strategy was more favorable for exposure of Co-N_x active sites and enhanced the MSD. To evaluate the intrinsic activity of Co-N_x, the site activity calculated by normalizing mass activity (MA) at 0.90 V vs RHE to MSD was deeply explored. As could be seen from Fig. 4a, dual-confined catalyst Co-ZIF8-PIL-800 achieved an outstanding MA of ~4.0 A·g⁻¹, which was 5.1, 8.2 and 12.2 times higher than that of Co-ZIF8-NGO-800, ZIF67-800 and Co-PIL-800, respectively. After normalized by MSD, the site activities of the corresponding catalysts were displayed in Fig. 4b, and Co-ZIF8-PIL-800 showed still relatively higher site activity of ~2.0 A·μmol⁻¹ than that of Co-ZIF8-NGO-800, ZIF67-800 and Co-PIL-800. Considering that Co-N_x species were the main ORR active sites for these Co-based catalysts, the site activities of them should be close to each other, which contradicted the experiment results. To deeply understand the reason behind the ORR performance enhancement of the as-prepared catalysts, the influence of N configuration on the Co-N_x active species was investigated. The concentration distribution of different N species was analysed and illustrated in Table S3. Compared with Co-PIL-800 and ZIF67-800 catalysts, the concentration of pyrrolic N in Co-ZIF8-PIL-800 decreased significantly, while the concentration of pyridinic N and graphitic N increased, which indicated that the introduction of ZIF-8 precursor could promote the conversion of pyrrolic N to pyridinic and graphitic N species. The pyridinic N was proved to be an effective species to coordinate with metal atom to create the M-N_x active sites [5,36,49]. The graphitic N was favourable to the electron transport. The concentration distribution of pyridinic N species in catalysts followed the order of Co-ZIF8-PIL-800 > ZIF67-800 > Co-PIL-800, which was in good agreement with the ORR activity of Co-N_x species. Thus, it can be deduced that not only the concentration of Co-N_x species but also the N configuration have significant influences on the ORR performance.

To verify the influence of the N configuration on the ORR activity, density functional theory (DFT) calculations were conducted based on the optimized pyridinic and pyrrolic N-coordinated Co-N₄-graphene model structures shown in Figs. 4c and d. Firstly, the ORR 4e transfer process was simulated on the two different N configuration coordinated Co-N₄-graphene models where four possible reaction routes happened including the hydrogenation of adsorbed O₂ (O₂*) to OOH*, the O-O bond cleavage of OOH* to O*, the protonation of O* to OH*, and the desorption of OH* on the active sites to generate OH⁻ (Fig. S21). The length of Co-O and O-O bond in the different adsorption states of intermediates (O₂*, OOH*, O*, and OH*) on the optimized pyridinic N-coordinated Co-N₄ model was longer than pyrrolic N-coordinated Co-N₄ model, indicating the relatively weak interaction between O species and active Co species, which might cause the easier reaction of the intermediates on pyridinic N-coordinated Co-N₄ species [43,50]. Furthermore, the free energy of different intermediates for the 4e ORR reaction processes were calculated to compare the catalytic performance

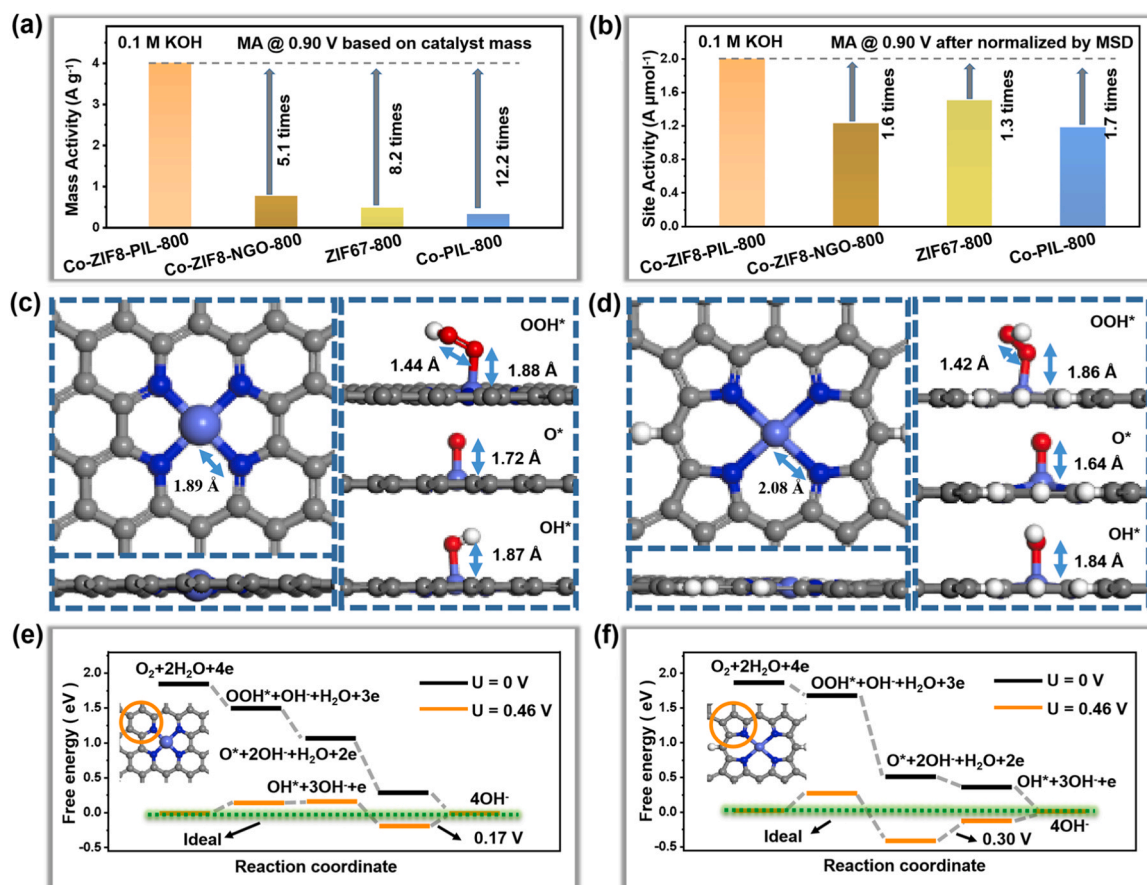


Fig. 4. Dissection and simulation of the intrinsic activity of Co-N_x species. (a) Mass activity at 0.90 V vs. RHE and (b) site activity at 0.9 V of Co-ZIF8-PIL-800, Co-ZIF8-NGO-800, ZIF67-800 and Co-PIL-800. Atomic configurations of (c) the pyridinic N-coordinated Co-N₄ species and the different adsorption states toward intermediates on the pyridinic N-coordinated Co-N₄ species and (d) pyrrolic N-coordinated Co-N₄ species and the different adsorption states toward intermediates on the pyrrolic N-coordinated Co-N₄ species. The calculated free energy pathways for the (e) pyridinic N-coordinated Co-N₄ species and (f) pyrrolic N-coordinated Co-N₄ species at U = 0 V and 0.46 V, respectively.

between the pyridinic N-coordinated Co-N₄ and pyrrolic N-coordinated Co-N₄ species as illustrated in Fig. 4e and f. At U = 0 V, the free energy routes on both pyridinic and pyrrolic N-coordinated Co-N₄ species are both downhill, which indicate that every electron transfer process during the ORR reaction is thermodynamically spontaneous [5]. The smaller negative free energy change (ΔG) on pyridinic N-coordinated Co-N₄ from the first reaction step ($O_2 + H_2O + e^- \rightarrow OOH^* + OH^*$) reveals that O_2 is more easily activated on the pyridinic N-coordinated Co-N₄ species. At U = 0.46 V, the computed overpotential of ORR on the pyridinic N-coordinated Co-N₄ species (0.17 eV) is still lower than that on the pyrrolic N-coordinated Co-N₄ species (0.3 eV). The green line represents the theoretical ideal free energy profile and the pyridinic N-coordinated Co-N₄ species possess the closest diagram to the ideal profile, meaning that the better ORR performance than the pyrrolic N-coordinated Co-N₄ species. These stimulation results clearly explained the activity difference of Co-base catalysts prepared through different methods was also affected by the difference of N configuration besides the exposure of Co-N_x species.

3.4.3. The Zn-air battery performance

The overall oxygen electrocatalytic activity can be assessed by the potential difference ($\Delta E = E_{j=10} - E_{1/2}$) in OER and ORR metrics, where a smaller ΔE means superior catalytic reversibility [43,51,52]. The overall ORR/OER performance of Co-ZIF8-PIL-800 was tested at a wide potential range from 0.3 to 1.8 V vs. RHE. As shown in Fig. 5a and Fig. S22, the Co-ZIF8-PIL-800 displayed not only superior ORR activity but also excellent OER performance ($E_{j=10} = 1.69$ V), and accordingly

the smallest ΔE value of ~0.82 V among the Co-based catalysts and noble-metal-based Pt/C + RuO₂ counterpart (ΔE = 0.85 V). Inspired by the superior ORR/OER bifunctional activity of Co-ZIF8-PIL-800, the liquid and flexible quasi-solid ZABs were assembled to evaluate the potential application under practical condition. As anticipated, the liquid ZAB catalysed by Co-ZIF8-PIL-800 displayed a narrower charging/discharging voltage gap and higher power density of 110.7 mW·cm⁻² than that catalysed by Pt/C + RuO₂ (Fig. 5b). Also, Co-ZIF8-PIL-800 ZAB yielded exceptional specific capacity of 810.9 mA h·g_{Zn}⁻¹ based on the mass of consumed Zn anode at 10 mA·cm⁻², which surpassed that of Pt/C + RuO₂ ZAB (756.3 mA h·g_{Zn}⁻¹) (Fig. 5c). In addition to activity, the rate capability and cycling stability are of vital significance for the practical implementation of ZABs. As shown in Fig. 5d and e, under different discharge current densities (2–10 mA·cm⁻²), Co-ZIF8-PIL-800 ZAB showed higher voltage plateaus with the stable discharge voltages and the voltage retention rate of 99.4% when the current was restored to 2 mA·cm⁻² after 14 h, and the long cycling stability with a voltage gap less than 963 mV after 650 cycles was observed. By contrast, the voltage plateaus were relatively lower and the voltage gap increased to 1200 mV at less than 300 cycles for Pt/C and RuO₂ ZAB. To broaden specific requirements during practical applications, flexible quasi-solid-state ZABs were further fabricated and studied. As shown in Fig. 5f, the flexible ZAB could still work stably for 60 cycles (10 h) at different bending angles ranging from 0° to 135° without obvious voltage gap expansion. Compared with previous reports, the Co-ZIF8-PIL-800 displayed excellent application prospects in the design of wearable electronic devices

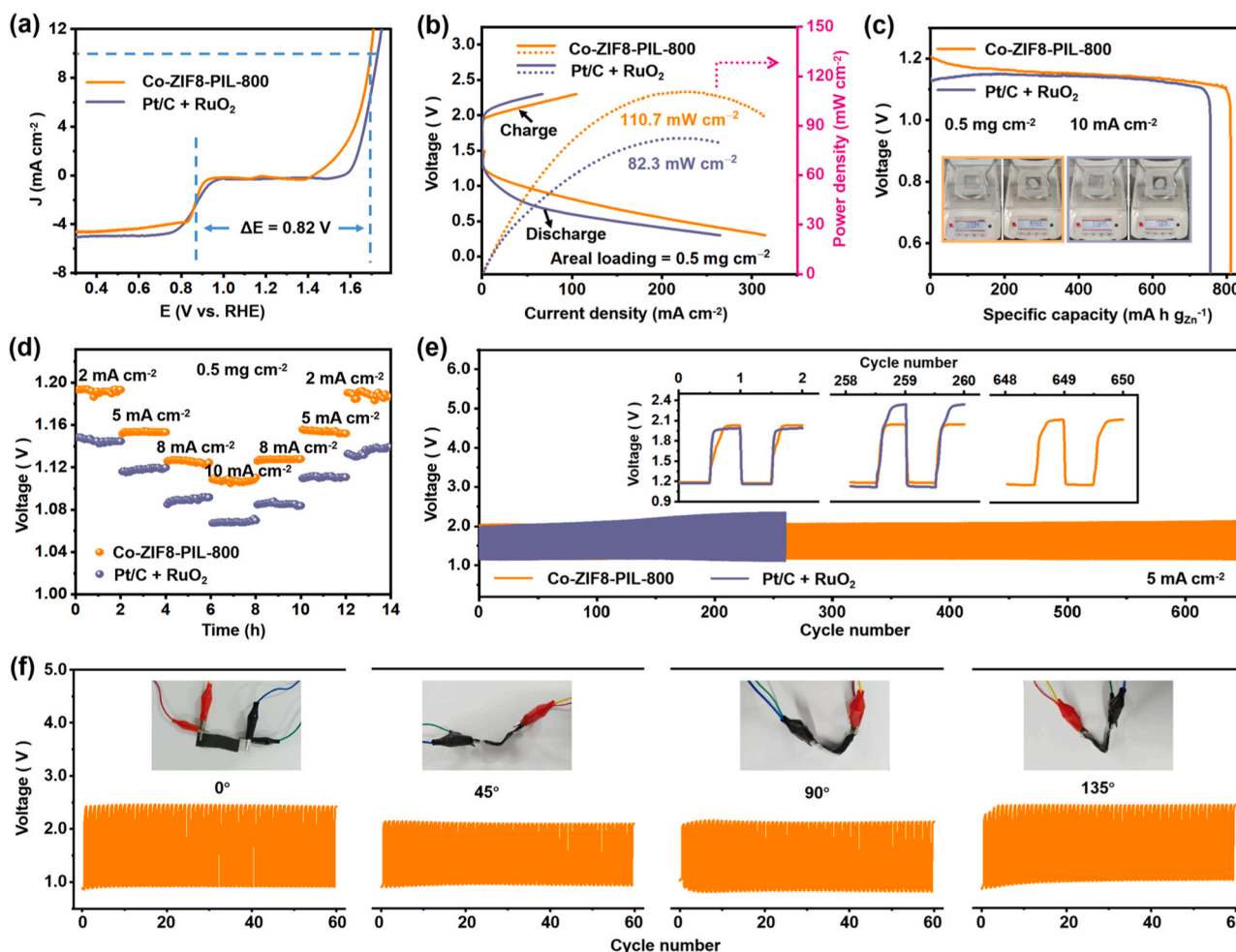


Fig. 5. Superior Zn-air battery performance of Co-ZIF8-PIL-800 catalyst to the benchmark 20% Pt/C+RuO₂. Performances comparison of (a) LSV curves tested in O₂-saturated 0.1 M KOH electrolyte at the scan rate of 5 mV s⁻¹ at the rotation speed of 1600 rpm; (b) Polarization and power density curves of the corresponding Zn-air batteries; (c) Specific capacity plots at current densities of 10 mA cm⁻², normalized via the mass of consumed Zn (inset); (d) Galvanostatic discharge curves of the Zn-air batteries at various current densities; (e) Galvanostatic discharge-charge cycling profiles at the current density of 5 mA cm⁻² with the scan rate of 600 s per cycle. (f) Galvanostatic discharge-charge cycling curve of Co-ZIF8-PIL-800 at 2 mA cm⁻² for the quasi-solid-state rechargeable Zn-air battery, applying bending strain (inset) every 3 h.

(Table S5). The excellent electrocatalysis activity, rate capacity and long cycling stability of Co-ZIF8-PIL-800 in liquid and flexible quasi-solid ZABs indicate that the unique 2D/3D dual-confined structure with abundant mesopore and high exposure of Co-N_x species promotes high intrinsic reactivity and mass transport, thereby results in the collective enhancement of oxygen electrocatalytic efficiency and cell performance.

4. Conclusions

In summary, Co-based hierarchical catalysts with highly accessible active sites and structural stability were facially prepared by 2D/3D dual-confined strategy with Co species being homogeneously confined into 3D ZIF-8 frameworks and jointly embedded into 2D lamellar poly (ionic liquid) (PIL) networks. The hierarchical 2D/3D composite structure with high mesoporosity increased the exposure of the Co-N_x active sites, and promoted the conversion of Co-pyrrolic N to Co-pyridinic N which was the main active species for ORR as verified by DFT calculations. As a result, the obtained Co-ZIF8-PIL-800 catalyst exhibited excellent ORR performance with E_{1/2} of 0.87 V, MA of 65.8 A·g⁻¹, TOF of 0.17 s⁻¹ and superior stability to that of commercial Pt/C (20 wt%) under alkaline conditions. When assembled as an oxygen cathode for liquid and flexible quasi-solid ZABs, Co-ZIF8-PIL-800 catalyst displayed superior specific capacity (810.9 mA h·g_{Zn}⁻¹ at 10 mA·cm⁻²) and

excellent long-cycling stability than benchmark Pt/C + RuO₂ catalyst, implying the potential prospects in the design of wearable electronics. This work not only designed a facial and effective strategy for the fabrication of transition-metal-based ORR catalysts with high performance for ZABs, but also systematically explored the reasons for the enhanced activity from the coordination environment and electron structure of Co-N_x active species, which may shed some light on the design of the efficient electrocatalysts.

CRediT authorship contribution statement

Yong-Ya Zhang, Shuang-Quan Zang: Conceptualization. **Jinping Zhang, Yong-Ya Zhang, Rui Wang:** Methodology. **Jinping Zhang, Zhiyuan Mei, Lilan Yi:** Data curation. **Kejian Li, Xincheng Hu:** TEM measurement. **Jinshu Tian, Yong-Ya Zhang:** Formal analysis. **Hong Guo, Rui Wang, Shuang-Quan Zang:** Supervision. **Jinping Zhang:** Writing – original draft. **Jinping Zhang, Yong-Ya Zhang, Shuang-Quan Zang:** Writing – review & editing.

Declaration of Competing Interest

The authors declare that they have no known competing financial interests or personal relationships that could have appeared to influence

the work reported in this paper.

Data availability

Data will be made available on request.

Acknowledgments

The authors greatly appreciate the financial support from the National Natural Science Foundation of China (No. 2182510, 22279115, 22104079), the Key Scientific Research Project of Colleges and Universities in Henan Province (22A150052), the Science and Technology Research Project of Henan Province (212102210654, 232102230085), and Henan Provincial Postdoctoral Science Foundation (202102004).

Appendix A. Supporting information

Supplementary data associated with this article can be found in the online version at [doi:10.1016/j.apcatb.2023.123044](https://doi.org/10.1016/j.apcatb.2023.123044).

References

- Z.L. Wang, D. Xu, J.J. Xu, X.B. Zhang, Oxygen electrocatalysts in metal-air batteries: from aqueous to nonaqueous electrolytes, *Chem. Soc. Rev.* 43 (2014) 7746–7786.
- M. Luo, Z. Zhao, Y. Zhang, Y. Sun, Y. Xing, F. Lv, Y. Yang, X. Zhang, S. Hwang, Y. Qin, J.Y. Ma, F. Lin, D. Su, G. Lu, S. Guo, PdMo bimetallic for oxygen reduction catalysis, *Nature* 574 (2019) 81–85.
- Y. Ma, J. Li, X. Liao, W. Luo, W. Huang, J. Meng, Q. Chen, S. Xi, R. Yu, Y. Zhao, L. Zhou, L. Mai, Heterostructure design in bimetallic phthalocyanine boosts oxygen reduction reaction activity and durability, *Adv. Funct. Mater.* 30 (2020) 2005000.
- J. Muñoz, C. Ifelsberger, E. Redondo, M. Pumera, Design of bimetallic 3D-printed electrocatalysts via galvanic replacement to enhance energy conversion systems, *Appl. Catal. B Environ.* 316 (2022), 121609.
- S. Liu, C. Li, M.J. Zachman, Y. Zeng, H. Yu, B. Li, M. Wang, J. Braaten, J. Liu, H. M. Meyer, M. Lucero, A.J. Kropf, E.E. Alp, Q. Gong, Q. Shi, Z. Feng, H. Xu, G. Wang, D.J. Myers, J. Xie, D.A. Cullen, S. Litster, G. Wu, Atomically dispersed iron sites with a nitrogen-carbon coating as highly active and durable oxygen reduction catalysts for fuel cells, *Nat. Energy* 7 (2022) 652–663.
- Q. Hu, G. Li, G. Li, X. Liu, B. Zhu, X. Chai, Q. Zhang, J. Liu, C. He, Trifunctional electrocatalysis on dual-doped graphene nanorings-integrated boxes for efficient water splitting and Zn-air batteries, *Adv. Energy Mater.* 9 (2019) 1803867.
- C. Vogt, B.M. Weckhuysen, The concept of active site in heterogeneous catalysis, *Nat. Rev. Chem.* 6 (2022) 89–111.
- T. Cui, L. Ma, S. Wang, C. Ye, X. Liang, Z. Zhang, G. Meng, L. Zheng, H.S. Hu, J. Zhang, H. Duan, D. Wang, Y. Li, Atomically dispersed Pt–N₃C sites enabling efficient and selective electrocatalytic C–C bond cleavage in lignin models under ambient conditions, *J. Am. Chem. Soc.* 143 (2021) 9429–9439.
- K.M. Zhao, S.Q. Liu, Y.Y. Li, X.L. Wei, G.Y. Ye, W.W. Zhu, Y.K. Su, J. Wang, H. T. Liu, Z. He, Z.Y. Zhou, S.G. Sun, Insight into the mechanism of axial ligands regulating the catalytic activity of Fe–N₄ sites for oxygen reduction reaction, *Adv. Energy Mater.* 12 (2022) 2103588.
- D. Liu, G. Xu, H. Yang, H. Wang, B.Y. Xia, Rational design of transition metal phosphide-based electrocatalysts for hydrogen evolution, *Adv. Funct. Mater.* 32 (2022) 2208358.
- J. Wu, Y. Huang, W. Ye, Y. Li, CO₂ reduction: from the electrochemical to photochemical approach, *Adv. Sci.* 4 (2017) 1700194.
- J. Masa, C. Andronescu, W. Schuhmann, Electrocatalysis as the nexus for sustainable renewable energy: the gordian knot of activity, stability, and selectivity, *Angew. Chem. Int. Ed.* 59 (2020) 15298–15312.
- X.X. Wang, V. Prabhakaran, Y. He, Y. Shao, G. Wu, Iron-free cathode catalysts for proton-exchange-membrane fuel cells: cobalt catalysts and the peroxide mitigation approach, *Adv. Mater.* 31 (2019), e1805126.
- T.W. Hansen, A.T. Delariva, S.R. Challa, A.K. Datye, Sintering of catalytic nanoparticles: particle migration or ostwald ripening? *Acc. Chem. Res.* 46 (2013) 1720–1730.
- W. Zhan, Y. Shu, Y. Sheng, H. Zhu, Y. Guo, L. Wang, Y. Guo, J. Zhang, G. Lu, S. Dai, Surfactant-assisted stabilization of Au colloids on solids for heterogeneous catalysis, *Angew. Chem. Int. Ed.* 56 (2017) 4494–4498.
- X. Yang, Q. Li, E. Lu, Z. Wang, X. Gong, Z. Yu, Y. Guo, L. Wang, Y. Guo, W. Zhan, J. Zhang, S. Dai, Taming the stability of Pd active phases through a compartmentalizing strategy toward nanostructured catalyst supports, *Nat. Commun.* 10 (2019) 1611–1619.
- H. Chen, K. Shen, Q. Mao, J. Chen, Y. Li, Nanoreactor of MOF-derived yolk-shell Co@C–N: precisely controllable structure and enhanced catalytic activity, *ACS Catal.* 8 (2018) 1417–1426.
- D. Liu, L. Dai, X. Lin, J.F. Chen, J. Zhang, X. Feng, K. Mullen, X. Zhu, S. Dai, Chemical approaches to carbon-based metal-free catalysts, *Adv. Mater.* 31 (2019), e1804863.
- Q. Xiong, J. Zheng, B. Liu, Y. Liu, H. Li, M. Yang, In-situ self-templating construction of FeNi/N co-doped 3D porous carbon from bimetallic ions-coordinated porous organic polymer for rechargeable zinc-air batteries, *Appl. Catal. B Environ.* 321 (2023), 122067.
- G. Chen, T. Wang, P. Liu, Z. Liao, H. Zhong, G. Wang, P. Zhang, M. Yu, E. Zschech, M. Chen, J. Zhang, X. Feng, Promoted oxygen reduction kinetics on nitrogen-doped hierarchically porous carbon by engineering proton-feeding centers, *Energy Environ. Sci.* 13 (2020) 2849–2855.
- J. Wu, F. Xu, S. Li, P. Ma, X. Zhang, Q. Liu, R. Fu, D. Wu, Porous polymers as multifunctional material platforms toward task-specific applications, *Adv. Mater.* 31 (2019), e1802922.
- Y. He, S. Hwang, D.A. Cullen, M.A. Uddin, L. Langhorst, B.Y. Li, S. Karakalos, A. J. Kropf, E.C. Wegener, J. Sokolowski, M.J. Chen, D. Myers, D. Su, K.L. More, G. F. Wang, S. Litster, G. Wu, Highly active atomically dispersed CoN₄ fuel cell cathode catalysts derived from surfactant-assisted MOFs: carbon-shell confinement strategy, *Energy Environ. Sci.* 12 (2019) 250–260.
- Y. Pan, K. Sun, S. Liu, X. Cao, K. Wu, W.C. Cheong, Z. Chen, Y. Wang, Y. Li, Y. Liu, D. Wang, Q. Peng, C. Chen, Y. Li, Core-shell ZIF-8@ZIF-67-derived CoP nanoparticle-embedded N-doped carbon nanotube hollow polyhedron for efficient overall water splitting, *J. Am. Chem. Soc.* 140 (2018) 2610–2618.
- H. Liu, J. Guan, S. Yang, Y. Yu, R. Shao, Z. Zhang, M. Dou, F. Wang, Q. Xu, Metal-organic-framework-derived Co₂P nanoparticle/multi-doped porous carbon as a trifunctional electrocatalyst, *Adv. Mater.* 32 (2020), e2003649.
- Z. Qiao, S. Hwang, X. Li, C. Wang, W. Samarakoon, S. Karakalos, D. Li, M. Chen, Y. He, M. Wang, Z. Liu, G. Wang, H. Zhou, Z. Feng, D. Su, J.S. Spendelow, G. Wu, 3D porous graphitic nanocarbon for enhancing the performance and durability of Pt catalysts: a balance between graphitization and hierarchical porosity, *Energy Environ. Sci.* 12 (2019) 2830–2841.
- J. Zhang, S. Nagamatsu, J. Du, C. Tong, H. Fang, D. Deng, X. Liu, K. Asakura, Y. Yuan, A study of FeN/C catalysts for the selective oxidation of unsaturated alcohols by molecular oxygen, *J. Catal.* 367 (2018) 16–26.
- Y.J. Wang, N. Zhao, B. Fang, H. Li, X.T. Bi, H. Wang, Carbon-supported Pt-based alloy electrocatalysts for the oxygen reduction reaction in polymer electrolyte membrane fuel cells: particle size, shape, and composition manipulation and their impact to activity, *Chem. Rev.* 115 (2015) 3433–3467.
- Y.Y. Zhang, N. Zhang, P. Peng, R. Wang, Y. Jin, Y.K. Lv, X. Wang, W. Wei, S. Q. Zhang, Uniformly dispersed Ru nanoparticles constructed by in-situ confined polymerization of ionic liquids for the electrocatalytic hydrogen evolution reaction, *Small Methods* 5 (2021), e2100505.
- D. Xie, Y. Xu, Y. Wang, X. Pan, E. Hark, Z. Kochovski, A. Eljarrat, J. Muller, C. T. Koch, J. Yuan, Y. Lu, Poly(ionic liquid) nanovesicle-templated carbon nanocapsules functionalized with uniform iron nitride nanoparticles as catalytic sulfur host for Li-S batteries, *ACS Nano* 16 (2022) 10554–10565.
- Z. Chen, Y. Ha, H. Jia, X. Yan, M. Chen, M. Li, R. Wu, Oriented transformation of Co-LDH into 2D/3D ZIF-67 to achieve Co–N–C hybrids for efficient overall water splitting, *Adv. Energy Mater.* 9 (2019) 1803918.
- X.X. Wang, D.A. Cullen, Y.T. Pan, S. Hwang, M. Wang, Z. Feng, J. Wang, M. H. Engelhard, H. Zhang, Y. He, Y. Shao, D. Su, K.L. More, J.S. Spendelow, G. Wu, Nitrogen-coordinated single cobalt atom catalysts for oxygen reduction in proton exchange membrane fuel cells, *Adv. Mater.* 30 (2018) 1706758.
- L. Shang, H. Yu, X. Huang, T. Bian, R. Shi, Y. Zhao, G.I. Waterhouse, L.Z. Wu, C. H. Tung, T. Zhang, Well-dispersed ZIF-derived Co₂N–Co doped carbon nanoframes through mesoporous-silica-protected calcination as efficient oxygen reduction electrocatalysts, *Adv. Mater.* 28 (2016) 1668–1674.
- W. Xia, M.A. Hunter, J. Wang, G. Zhu, S.J. Warren, Y. Zhao, Y. Bando, D.J. Searles, Y. Yamauchi, J. Tang, Highly ordered macroporous dual-element-doped carbon from metal-organic frameworks for catalyzing oxygen reduction, *Chem. Sci.* 11 (2020) 9584–9592.
- G. Wu, K.L. More, C.M. Johnston, P. Zelenay, High-performance electrocatalysts for oxygen reduction derived from polyaniline, iron, and cobalt, *Science* 332 (2011) 443–447.
- Q. Cheng, S. Han, K. Mao, C. Chen, L. Yang, Z. Zou, M. Gu, Z. Hu, H. Yang, Co nanoparticle embedded in atomically-dispersed Co–N–C nanofibers for oxygen reduction with high activity and remarkable durability, *Nano Energy* 52 (2018) 485–493.
- H.W. Liang, S. Bruller, R. Dong, J. Zhang, X. Feng, K. Mullen, Molecular metal–N_x centres in porous carbon for electrocatalytic hydrogen evolution, *Nat. Commun.* 6 (2015) 7992–7999.
- Y. Yang, R. Zeng, Y. Xiong, F.J. DiSalvo, H.D. Abruna, Cobalt-based nitride-core oxide-shell oxygen reduction electrocatalysts, *J. Am. Chem. Soc.* 141 (2019) 19241–19245.
- J. Sun, P. Leng, Y. Xie, X. Yu, K. Qu, L. Feng, H. Bao, F. Luo, Z. Yang, Co single atoms and Co nanoparticle relay electrocatalyst for rechargeable zinc air batteries, *Appl. Catal. B Environ.* 319 (2022), 121905.
- P. Yu, L. Wang, F. Sun, Y. Xie, X. Liu, J. Ma, X. Wang, C. Tian, J. Li, H. Fu, Co nanoislands rooted on Co–N–C nanosheets as efficient oxygen electrocatalyst for Zn–air batteries, *Adv. Mater.* 31 (2019), e1901666.
- W. Cheng, P. Yuan, Z. Lv, Y. Guo, Y. Qiao, X. Xue, X. Liu, W. Bai, K. Wang, Q. Xu, J. Zhang, Boosting defective carbon by anchoring well-defined atomically dispersed metal–N₄ sites for ORR, OER, and Zn-air batteries, *Appl. Catal. B Environ.* 260 (2020), 118198.
- Y.P. Deng, Y. Jiang, R. Liang, S.J. Zhang, D. Luo, Y. Hu, X. Wang, J.T. Li, A. Yu, Z. Chen, Dynamic electrocatalyst with current-driven oxyhydroxide shell for rechargeable zinc-air battery, *Nat. Commun.* 11 (2020) 1952–1961.
- Y. Jiang, Y.P. Deng, R. Liang, J. Fu, R. Gao, D. Luo, Z. Bai, Y. Hu, A. Yu, Z. Chen, d-Orbital steered active sites through ligand editing on heterometal imidazole

- frameworks for rechargeable zinc-air battery, *Nat. Commun.* 11 (2020) 5858–5868.
- [43] G. Yang, J. Zhu, P. Yuan, Y. Hu, G. Qu, B.A. Lu, X. Xue, H. Yin, W. Cheng, J. Cheng, W. Xu, J. Li, J. Hu, S. Mu, J.N. Zhang, Regulating Fe-spin state by atomically dispersed Mn-N in Fe–N–C catalysts with high oxygen reduction activity, *Nat. Commun.* 12 (2021) 1734–1743.
- [44] F. Dionigi, J. Zhu, Z. Zeng, T. Merzdorf, H. Sarodnik, M. Gliech, L. Pan, W.X. Li, J. Greeley, P. Strasser, Intrinsic electrocatalytic activity for oxygen evolution of crystalline 3d-transition metal layered double hydroxides, *Angew. Chem. Int. Ed.* 60 (2021) 14446–14457.
- [45] L. Chen, X. Liu, L. Zheng, Y. Li, X. Guo, X. Wan, Q. Liu, J. Shang, J. Shui, Insights into the role of active site density in the fuel cell performance of Co–N–C catalysts, *Appl. Catal. B Environ.* 256 (2019), 117849.
- [46] X. Wang, Z. Chen, Z. Han, H. Gai, J. Zhou, Y. Wang, P. Cui, J. Ge, W. Xing, X. Zheng, M. Huang, H. Jiang, Manipulation of new married edge-adjacent Fe₂N₅ catalysts and identification of active species for oxygen reduction in wide pH range, *Adv. Funct. Mater.* 32 (2022) 2111835.
- [47] D. Malko, A. Kucernak, T. Lopes, In situ electrochemical quantification of active sites in Fe–N/C non-precious metal catalysts, *Nat. Commun.* 7 (2016) 13285–13291.
- [48] S.H. Yin, S.L. Yang, G. Li, G. Li, B.W. Zhang, C.T. Wang, M.S. Chen, H.G. Liao, J. Yang, Y.X. Jiang, S.G. Sun, Seizing gaseous Fe²⁺ to densify O₂-accessible Fe–N₄ sites for high-performance proton exchange membrane fuel cells, *Energy Environ. Sci.* 15 (2022) 3033–3040.
- [49] W. Liu, L. Zhang, X. Liu, X. Liu, X. Yang, S. Miao, W. Wang, A. Wang, T. Zhang, Discriminating catalytically active FeN_x species of atomically dispersed Fe–N–C catalyst for selective oxidation of the C–H bond, *J. Am. Chem. Soc.* 139 (2017) 10790–10798.
- [50] B. Wang, Y. Hu, W. Liu, Y. Zhao, R. Yang, Z. Li, J. Luo, B. Chi, Z. Jiang, M. Li, S. Mu, S. Liao, J. Zhang, X. Sun, Isolated Zn-Co atomic pair for highly active and durable oxygen reduction, *Angew. Chem. Int. Ed.* 58 (2019) 2622–2626.
- [51] Y. Jiang, Y.P. Deng, R. Liang, N. Chen, G. King, A. Yu, Z. Chen, Linker-compensated metal-organic framework with electron delocalized metal sites for bifunctional oxygen electrocatalysis, *J. Am. Chem. Soc.* 144 (2022) 4783–4791.
- [52] Y. Zhang, Z. Zhang, G. Jiang, A.H. Mamaghani, S. Sy, R. Gao, Y. Jiang, Y. Deng, Z. Bai, L. Yang, A. Yu, Z. Chen, Three-dimensionally ordered mesoporous Co₃O₄ decorated with Mg as bifunctional oxygen electrocatalysts for high-performance zinc-air batteries, *Nano Energy* 100 (2022), 107425.